




Article

A Novel Membrane-like 2D A'-MoS₂ as Anode for Lithium- and Sodium-Ion Batteries

Ekaterina V. Sukhanova^{1,*} , Liudmila A. Bereznikova¹, Anton M. Manakhov^{2,*} , Hassan S. Al Qahtani³ and Zakhar I. Popov^{1,4,*} 

¹ Laboratory of Acoustic Microscopy, Emanuel Institute of Biochemical Physics RAS, 119334 Moscow, Russia

² Aramco Innovations LLC, Aramco Research Center, 119234 Moscow, Russia

³ EXPEC Advanced Research Centre, Saudi Aramco, Dhahran 31311, Saudi Arabia

⁴ Academic Department of Innovative Materials and Technologies Chemistry, Plekhanov Russian University of Economics, 117997 Moscow, Russia

* Correspondence: yekaterina.sukhanova@phystech.edu (E.V.S.);

anton.manakhov@aramcoinnovations.com (A.M.M.); zipcool@bk.ru (Z.I.P.)

Abstract: Currently, new nanomaterials for high-capacity lithium-ion batteries (LIBs) and sodium-ion batteries (SIBs) are urgently needed. Materials combining porous structure (such as representatives of metal-organic frameworks) and the ability to operate both with lithium and sodium (such as transition-metal dichalcogenides) are of particular interest. Our work reports the computational modelling of a new A'-MoS₂ structure and its application in LIBs and SIBs. The A'-MoS₂ monolayer was dynamically stable and exhibited semiconducting properties with an indirect band gap of 0.74 eV. A large surface area, together with the presence of pores resulted in a high capacity of the A'-MoS₂ equal to ~391 mA·g⁻¹ at maximum filling for both Li and Na atoms. High adsorption energies and small values of diffusion barriers indicate that the A'-MoS₂ is promising in the application of anode material in LIBs and SIBs.

Keywords: DFT; VASP; TMD; LIB; SIB; MoS₂ membrane



Citation: Sukhanova, E.V.; Bereznikova, L.A.; Manakhov, A.M.; Al Qahtani, H.S.; Popov, Z.I. A Novel Membrane-like 2D A'-MoS₂ as Anode for Lithium- and Sodium-Ion Batteries. *Membranes* **2022**, *12*, 1156. <https://doi.org/10.3390/membranes12111156>

Academic Editor: Ivo F. J. Vankelecom

Received: 21 October 2022

Accepted: 14 November 2022

Published: 16 November 2022

Publisher's Note: MDPI stays neutral with regard to jurisdictional claims in published maps and institutional affiliations.



Copyright: © 2022 by the authors. Licensee MDPI, Basel, Switzerland. This article is an open access article distributed under the terms and conditions of the Creative Commons Attribution (CC BY) license (<https://creativecommons.org/licenses/by/4.0/>).

1. Introduction

Metal-ion batteries are currently the main power source for electronic devices due to their high specific capacity [1,2]. Lithium-ion batteries (LIBs) are the most widely used [3] for many reasons such as their high energy density and the absence of memory effects [4]. Meanwhile, the widespread availability and low cost of sodium, which has a close value of redox potential (only ~0.3 V higher than lithium) and is characterized by the similar chemistry of ion intercalation, make sodium-ion batteries (SIBs) no less attractive than LIBs [5,6]. On the one hand, SIBs can serve as an excellent alternative to the LIBs taking into account the reduced availability of lithium and some shortages affecting their application [3,7,8]. On the other hand, Na⁺ ions have a larger radius, which directly affects the mass transfer and the energy storage in the electrochemical process [9].

Layered bulk structures consisting of two-dimensional monolayers can act as effective anode materials due to the rapid transport of ions in the interlayer space and the large surface area which improves the adsorption of particles [10–13]. For example, at this moment, graphite, with a layered structure, is the most widely implemented anode material for LIBs [14] and is characterized by a high theoretical capacity of 372 mA·h·g⁻¹ for Li atoms (by forming LiC₆) [15]. Graphite electrodes have a long service life [16]; however, they are characterized by a low range of operating temperatures [17]. In the case of SIBs, the graphite's value of electrochemical capacity is less than 35 mA·h·g⁻¹ [18,19] which was attributed to the fact that the graphite's interlayer distance (~0.34 nm) is too small to accommodate Na⁺ ions (the minimum required distance is 0.37 nm [20]). Moreover, the Na–C chemical bond is less covalent compared to the Li–C bond [21], and, as a result, Na–C

compounds are thermodynamically unstable [21,22]. However, alkali-metal ions with large atomic numbers (such as K^+ ions) can form energetically favorable configurations in graphite sheets [23,24], but the high values of these ion masses make their use in metal-ion batteries less favorable. In this regard, current research is focused on the development of new electrode materials, first, to overcome limitations and eliminate, for example, shortcomings in both LIBs and SIBs [25] and second, to improve the characteristics of the existing devices. Carbon-based materials are an attractive platform to enhance metal-ion battery performance. For example, yolk-shell ZnS@C structures for Li- and K-ion storage [26] and porous FeS@N-doped carbon nanosheets for Na- and K-ion storage [27] demonstrate high capacity, but their use requires complex approaches to the synthesis.

The transition-metal dichalcogenides (TMDs) are applicable for both LIBs and SIBs [28]. The interlayer space in bulk TMDs and the weak van der Waals forces between the layers provide not only a large number of intercalation channels for metal ions but also a rapid diffusion of particles between the layers [29–31]. However, TMDs are characterized by lower theoretical capacity compared with graphite due to the larger molecular weight of the elements forming the structure. For example, bulk 2H-MoS₂ has a value of 167 mAh·g^{−1} (considering one Li atom per one MoS₂ formal unit) [32]. This capacity can be increased by two times by switching to a monolayer MoS₂ (two Li atoms per one MoS₂ formal unit) [33]. However, a further increase of capacity characteristics requires the application of artificial approaches, such as composite construction [34,35]. The second possible approach is the complete decomposition of MoS₂ accompanied by the formation of Li₂S (Na₂S) and Li-Mo (Na-Mo) alloys. However, this method will complicate the reverse transition and reflect poorly on the cyclicity [32,36,37]. In addition, there is an alternative approach which is the search for new phases of TMDs having less density than H-MoS₂ monolayers because bulk TMDs can exist not only in the hexagonal 2H phase but also in trigonal 1T and rhombohedral 3R polymorphs [38]. Moreover, recent investigations showed that transition-metal chalcogenides can form various monolayered structures [39–44].

Another interesting class of compounds that are promising materials for lithium-ion batteries are metal-organic frameworks (MOFs) due to their tunable porosity, high surface area, and abundant cavities reducing the strain during charging and discharging processes, resulting in increased service life [45–47]. The direct utilization of MOFs as anodes in SIBs is hindered by poor electrical conductivity and instability in organic electrolytes [46], but some MOF derivatives are deprived of such shortcomings [46,48]. Despite all the advantages of MOFs, their application is still limited due to the ambiguous principles of their design and insufficient knowledge of the material.

The ability of TMDs to act as an anode in both LIBs and SIBs can be improved by creating a porous structure inspired by MOFs. In the present work, the membrane-like structure of the A'-MoS₂ monolayer was theoretically examined in terms of application as an anode material for LIBs and NIBs.

2. Methods

In this work, all quantum-chemical calculations were based on density-functional theory (DFT) [49,50] and performed within the VASP [51–55] program package. The projected augmented wave (PAW) [56] method was used to describe the interactions between electrons and ion cores. The exchange-correlation functional was calculated via generalized gradient approximation (GGA) in Perdew–Burke–Ernzerhof (PBE) parameterization [57]. The energy cutoff of plane waves was set to be equal to 400 eV. To investigate the dependence of the alkali metal (lithium and sodium) absorption and diffusion on the MoS₂ surface on the concentration we considered a unit cell of A'-MoS₂ consisting of 12 sulfur and 6 molybdenum atoms. The first Brillouin zone was sampled according to the Monkhorst–Pack scheme [58], and the k-point mesh of 5 × 3 × 1 was chosen. The relaxation of the atomic geometry was carried out until the maximum values of the energy difference between two electronic steps became less than 10^{−6} eV and between two ionic steps, 10^{−3} eV. The Grimme corrections (DFT-D3) [59] were applied to take into account

van der Waals interaction. To avoid the interactions between the periodic images we used a vacuum region of at least 15 Å in non-periodic directions. We used the elastic-band method (NEB) [60,61] combined with DFT calculations to investigate the minimal in energy diffusion pathways. To estimate the dynamic stability of A'-MoS₂ monolayers we studied the vibrational properties via phonon dispersion calculations based on the density functional perturbation theory. The force-constant matrix was calculated for the 2 × 2 × 1 supercell in the PHONOPY software package [62]. To take into account the crystal symmetry and get rid of the "overdetermination" of the system, the resulting matrix was processed using machine learning algorithms implemented in the Hiphive software package [63]. The VESTA [64] software was used for atomic structure visualization.

3. Results

In our work, we considered the MoS₂ monolayer in the A' phase, the structure of which was firstly proposed by Gavryushkin et al. [39] for Janus TMDs. The A'-MoS₂ monolayer is characterized by rhombic symmetry and belongs to the Pmn₂1 space group with the unit cell vectors of $a = 6.42$ Å and $b = 9.79$ Å. The feature of the A'-MoS₂ structure is the presence of ordered pores resulting in a lower area density of $2.54 \cdot 10^{-7}$ g·cm⁻² compared with the values for known H ($3.03 \cdot 10^{-7}$ g·cm⁻²) and T ($3.04 \cdot 10^{-7}$ g·cm⁻²) phases. The unit cell contains two pores that are equivalent but mirrored concerning the ab plane (see Figure 1a red and blue) which leads to the increase of the surface area and facilitates the possibility of the alkali-metal atoms' diffusion in the perpendicular direction to the layer since the covalent radius of Li and Na atoms is less than the pore diameter. This feature provides more opportunities for the intercalation of alkali-metal atoms and makes the considered structure promising for use as an anode material in metal-ion batteries.

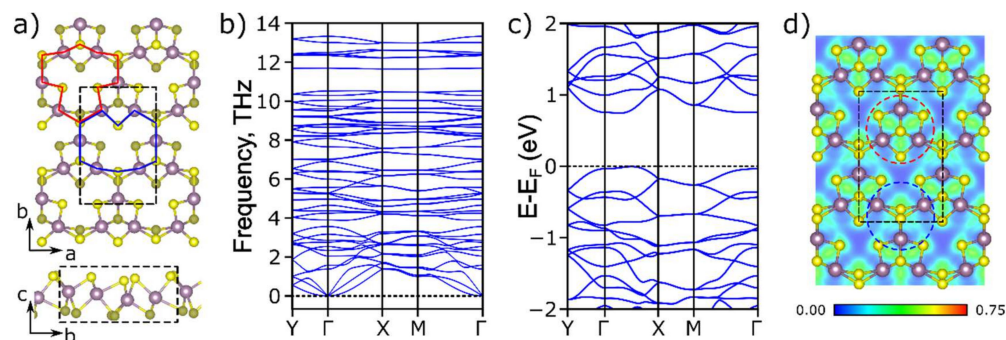


Figure 1. (a) Atomic structure, (b) phonon dispersion spectra, (c) electronic band structure, and (d) electron localization function for the total electron density along the ab plane for A'-MoS₂. The unit cell is indicated by black dashed lines. Mo and S atoms are depicted in purple and yellow colors, respectively. Two types of pores in the A'-MoS₂ structure are marked by red and blue areas in (a).

The dynamic stability of the A'-MoS₂ was investigated by phonon dispersion spectra calculation (see Figure 1b), and the absence of imaginary frequencies revealed the stability of the considered structure. To study the electronic properties of the A'-MoS₂ we calculated the density of electronic states and the electronic band structure along the path of $\Gamma(0, 1/2, 0) \rightarrow \Gamma(0, 0, 0) \rightarrow X(1/2, 0, 0) \rightarrow M(1/2, 1/2, 0) \rightarrow \Gamma(0, 0, 0)$ (see Figure 1c). The monolayer was shown to exhibit semiconducting electronic properties with an indirect band gap of 0.74 eV. In comparison, H-MoS₂ is a semiconductor with a band gap of 1.71 eV, while the T phase is a metal [65]. The p -states of the sulfur atom and the molybdenum d -states made the main contribution to the valence bond minimum, while the conduction band minima were mainly connected with Mo d -states (see Supplementary Figure S1). The semiconducting nature of the A'-MoS₂ can be attributed to two types of Mo–Mo interactions presented in the structure and associated with different bond lengths. The electron localization function (ELF) [66] displayed a non-zero value on the Mo–Mo bond with the length of 2.73 Å (see Figure 1d, red circle) which indicates the existence of an

interaction between these molybdenum atoms also observed in the metallic T phase [67]. On the contrary, in the case of Mo atoms with a bond length of 3.18 and 3.64 Å (see Figure 1d, blue circle) the interaction between Mo atoms was significantly less and the ELF pattern was close to the case of the H phase [68]. Based on the ELF analysis one can conclude that the semiconducting nature of the A'-MoS₂ arises from the weak Mo–Mo interaction between isolated Mo₃S₄ clusters connected through sulfur bridges. The small bandgap of the A' structure compared to the H phase makes it more convenient for metal-ion batteries due to low barrier electron transfer.

To investigate the alkali metal diffusion on the surface of the monolayer the intermediate positions of single alkali-metal atoms corresponding to a local energy minimum on the A'-MoS₂ structure were evaluated. We considered the positions above the molybdenum atoms (positions P2, P4, and P5), above the sulfur atoms (positions P1, P3, P6, and P7), and in the center of the pore (P8) as indicated in Figure 2a,b.

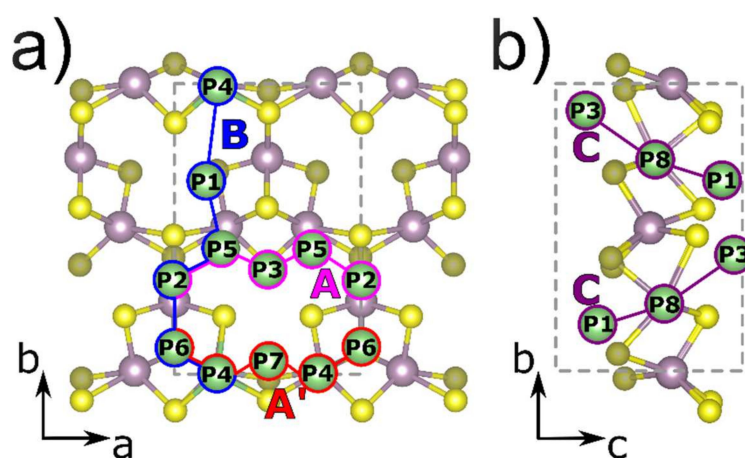


Figure 2. The considered positions of alkali-metal atom (Li, Na) adsorption on the surface of the A'-MoS₂ monolayer and the diffusion pathways: (a) A (pink) and B (blue), (b) C (red) and D (violet). The unit cell is indicated by the grey dashed lines. Mo, S, and alkali-metal atoms (Li, Na) are depicted in purple, yellow, and green colors, respectively.

We calculated the corresponding adsorption energies of a single Li/Na atom (E_{ads}) as:

$$E_{ads} = E_{MoS_2+1AM} - E_{MoS_2} - E_{AM}, \quad (1)$$

where E_{MoS_2} and E_{MoS_2+1Me} are the total energies of pristine 1A'-MoS₂ and 1A'-MoS₂ with adsorbed alkali-metal atom, and E_{AM} is the chemical potential of an alkali-metal (AM) atom (Li/Na) calculated from the corresponding BCC crystal. The obtained values of a single alkali-metal atom are presented in Table 1. The negative value of the adsorption energy indicates that it is more energetically favorable for alkali-metal atoms to be adsorbed onto the MoS₂ surface than to form a crystal.

The most energetically favorable position for both Li and Na atom adsorption corresponds to the position P1 above the three sulfur atoms forming the pore. The most unfavorable site for the Li atom is P7 above a sulfur triangle near the pore. The position P8 in the center of the pore and P6 above the central sulfur in the Mo₃S₃ cluster is the second most favorable for lithium atoms while for sodium atoms the position in the center of the pore is the most energetically unfavorable due to steric factors. In all considered cases the adsorption energy was negative meaning that the process of lithium and sodium storage on the surface of A'-MoS₂ was exothermic. The whole set of calculated positions corresponds to local minima of energy through which the diffusion of alkali-metal atoms can be considered.

Table 1. The adsorption energy of a single alkali-metal atom on the A'-MoS₂ surface and the energy difference calculated relative to position P1.

Position	E_{ads} (eV)		Relative Energy (eV)	
	Li	Na	Li	Na
P1	-1.22	-1.18	0.00	0.00
P2	-1.00	-0.87	0.25	0.35
P3	-1.01	-0.93	0.21	0.25
P4	-0.91	-0.80	0.31	0.39
P5	-0.99	-0.93	0.24	0.26
P6	-1.04	-0.86	0.19	0.34
P7	-0.79	-0.16	0.43	0.48
P8	-1.03	-0.43	0.19	0.71

All possible pathways of alkali-atom diffusion via corresponding positions on the A'-MoS₂ surface were considered: two paths along *a* direction of the structure P2→P5→P3→P5→P2 (denoted as A-path, see Figure 2a, pink) and P6→P4→P7→P4'→P6' (denoted as A'-path, see Figure 2a, blue), the path along *b* direction of the monolayer P4→P1→P5→P2→P6→P4 (denoted as B-path, see Figure 2a, red), as well as perpendicular to the slab surface direction via pore P1→P8→P3 (denoted as C-path, see Figure 2b, violet). Considered diffusion energy profiles are presented in Fig S2. The A-path was the most energetically favorable with the maximum barrier value of 0.16 eV for Li and 0.13 eV for Na atoms between P5 and P2 local minima (see Table 2). The A'-path was limited by the transition from P4 to P7 local minima (0.21 eV for Li and 0.14 for Na) and the P7 was the least energetically favorable among considered positions on the surface of A'-MoS₂ for both Li and Na atoms (see Table 2). The B-path was limited by transitions from P1 local minimum, which was the most energetically favorable position, by barriers from P1 to P4 (0.46 eV for Li and 0.50 eV for Na) in one direction and from P1 to P5 (0.40 eV for Li and 0.35 for Na) in the reverse direction (see Table 2). Considering the obtained values of diffusion barriers one can conclude that the diffusion of alkali-metal atoms on the surface of A'-MoS₂ has an anisotropic character and is more likely to occur in the A and A' directions than in the B direction. In the case of Li-atom diffusion on the surface of the A'-MoS₂, the obtained values of diffusion barriers were lower than for H-MoS₂ (0.57 eV [69]), while in the case of Na atom the values for A'-MoS₂ slightly exceeded the corresponding value for H-MoS₂ (0.28 eV [69]). In contrast to H-MoS₂, the structure of A'-MoS₂ contains pores, therefore, there is an additional diffusion direction perpendicular to the surface (C-path) for this structure. The diffusion through the pore following the C-path is associated with a local minimum P8, which, in the case of sodium, differed significantly from the most energetically favorable position P1 at 0.71 eV. In addition, to advance the Na atom into the pore relatively high energy barriers must be overcome (1.05 eV from P3 to P8 and 0.82 eV from P1 to P8) because of the steric factor correlated with a bigger ionic radius of the sodium atom compared to the lithium atom. In the case of the lithium atom diffusion through the P8 position, the diffusion barriers were less than through the P1 position along the B-path (see Table 2) which allows us to conclude that Li atoms can exhibit mobility not only on the surface of the A'-MoS₂ but also can overcome jumps between the slab surfaces.

Table 2. The energy-barrier values for the diffusion of alkali-metal atom (Li or Na) on the surface of the A'-MoS₂ monolayer and through the pore.

Transition Path			Li		Na	
			Direct	Reverse	Direct	Reverse
On the surface	A	P2→P5	0.16	0.16	0.06	0.13
		P5→P3	0.11	0.13	0.06	0.05
	A'	P6→P4	0.19	0.07	0.08	0.02
		P4→P7	0.21	0.09	0.14	0.04
	B	P4→P1	0.14	0.46	0.11	0.50
		P1→P5	0.40	0.17	0.35	0.10
		P5→P2	0.16	0.16	0.13	0.06
		P2→P6	0.21	0.26	0.16	0.15
		P6→P4	0.19	0.07	0.08	0.02
	Through the slab	C	P3→P8	0.22	0.38	1.05
P8→P1			0.22	0.28	0.07	0.82

To estimate the electrochemical performance of A'-MoS₂ anodes we calculated the open circuit voltage (OCV) and the value of the theoretical capacity (C). The OCV was calculated as:

$$OCV = -\frac{\Delta E}{nze} = -\frac{E_{A'}[MoS_2 + nMe] - E_{A'}[MoS_2] - nE[Me]}{nze}, \tag{2}$$

where $E_{A'}[MoS_2 + nMe]$ and $E_{A'}[MoS_2]$ are the total energies of A'-MoS₂ before and after n alkali-metal atoms adsorption, z is the electronic charge of metal ions (in the case of Li and Na atoms $z = 1$), and e represent electron charge, while the value of theoretical capacity (C) in mA·h·g⁻¹ was calculated using the formula:

$$C = 10^3 \frac{znF}{M_{A'}}, \tag{3}$$

where F is the Faraday constant ($F = 26.801 \text{ A} \cdot \text{h} \cdot \text{mol}^{-1}$) and $M_{A'}$ is the mole weight of the A'-MoS₂ unit cell. The OCV profile as a function of theoretical capacity (C) for Li and Na atoms is shown in Figure 3.

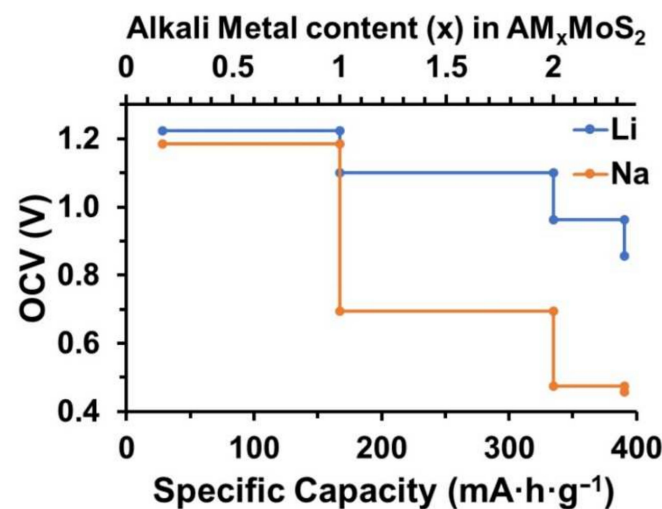


Figure 3. The open circuit voltage profile for A'-MoS₂ as a function of the theoretical capacity of Li (blue) and Na (orange).

The OCV for the A'-MoS₂ monolayer for both Li and Na was higher in comparison to the pristine H-MoS₂ monolayer [69] at the same range of capacities due to higher absorption

energy of alkali-metal atoms and was close to the values for defective H-MoS₂ containing Mo vacancies [69]. The highest value of A'-MoS₂ specific capacity denoted to the unit cell (Mo₆S₁₂) with 14 alkali-metal atoms was equal to 390.65 mA·h·g⁻¹ for both Li and Na which exceeds the value for the pristine H-MoS₂ monolayer [32,33,70]. The same value of maximum specific capacity for Na and for Li provided by the A'-MoS₂ area density makes the A'-MoS₂ membrane promising not only for LIBs and but also for SIBs without capacity loss.

4. Conclusions

To summarize, the novel porous A'-MoS₂ monolayer was investigated via DFT calculations. The membrane-like structure of A'-MoS₂ made possible Li and Na diffusion in all directions, but Na diffusion through the pore was limited by the high value of the diffusion barrier (1.05 eV) due to the steric factor. At the same time, the barrier for Li atom (0.38 eV) was lower than the highest one for diffusion on the surface (0.46 eV). The OCV values of the novel A'-MoS₂ monolayer were found to be in the same range as H-MoS₂ with Mo vacancies. The theoretical specific capacity was ~391 mA·h·g⁻¹, which was 17% higher than the maximum filling of 1T and 2H phases (~334 mA·h·g⁻¹) by Li atoms. Due to area density, the Na atom can fill the A'-MoS₂ monolayer with a same specific capacity which characterized the A' phase as a good candidate for the anode in LIBs/SIBs.

Supplementary Materials: The following supporting information can be downloaded at: <https://www.mdpi.com/article/10.3390/membranes12111156/s1>, Figure S1: Density of electronic state structures resolved by d-orbitals for Mo atoms and by p-orbitals for S atoms for A'-MoS₂; Figure S2: Diffusion energy profiles for Li (blue) and Na (orange) atoms' diffusion barriers in different considered directions for A'-MoS₂.

Author Contributions: Conceptualization, Z.I.P.; investigation, L.A.B., E.V.S. and Z.I.P.; writing—original draft preparation, L.A.B. and E.V.S.; writing—review and editing E.V.S., Z.I.P., A.M.M. and H.S.A.Q. All authors have read and agreed to the published version of the manuscript.

Funding: This research received no external funding.

Institutional Review Board Statement: Not applicable.

Data Availability Statement: Not applicable.

Acknowledgments: The authors are grateful to the Emanuel Institute of Biochemical Physics and the Joint Supercomputer Center of the Russian Academy of Sciences for providing access to the cluster computational resources.

Conflicts of Interest: The authors declare no conflict of interest.

References

1. Liang, Y.; Dong, H.; Aurbach, D.; Yao, Y. Current Status and Future Directions of Multivalent Metal-Ion Batteries. *Nat. Energy* **2020**, *5*, 646–656. [CrossRef]
2. Shea, J.J.; Luo, C. Organic Electrode Materials for Metal Ion Batteries. *ACS Appl. Mater. Interfaces* **2020**, *12*, 5361–5380. [CrossRef] [PubMed]
3. Nitta, N.; Wu, F.; Lee, J.T.; Yushin, G. Li-Ion Battery Materials: Present and Future. *Mater. Today* **2015**, *18*, 252–264. [CrossRef]
4. Lee, H.-M.; Ghovanloo, M. Energy management integrated circuits for wireless power transmission. In *Implantable Biomedical Microsystems*; Bhunia, S., Majerus, S., Sawan, M., Eds.; Elsevier: Amsterdam, The Netherlands, 2015; pp. 87–111. ISBN 978-0-323-26208-8.
5. Tarascon, J.-M. Key Challenges in Future Li-Battery Research. *Philos. Trans. R. Soc. A Math. Phys. Eng. Sci.* **2010**, *368*, 3227–3241. [CrossRef] [PubMed]
6. Nayak, P.K.; Yang, L.; Brehm, W.; Adelhelm, P. From Lithium-Ion to Sodium-Ion Batteries: Advantages, Challenges, and Surprises. *Angew. Chem. Int. Ed.* **2018**, *57*, 102–120. [CrossRef]
7. Slater, M.D.; Kim, D.; Lee, E.; Johnson, C.S. Sodium-Ion Batteries. *Adv. Funct. Mater.* **2013**, *23*, 947–958. [CrossRef]
8. Ellis, B.L.; Nazar, L.F. Sodium and Sodium-Ion Energy Storage Batteries. *Curr. Opin. Solid State Mater. Sci.* **2012**, *16*, 168–177. [CrossRef]
9. Eftekhari, A.; Kim, D.-W. Sodium-Ion Batteries: New Opportunities beyond Energy Storage by Lithium. *J. Power Sources* **2018**, *395*, 336–348. [CrossRef]

10. Peng, L.; Zhu, Y.; Chen, D.; Ruoff, R.S.; Yu, G. Two-Dimensional Materials for Beyond-Lithium-Ion Batteries. *Adv. Energy Mater.* **2016**, *6*, 1600025. [[CrossRef](#)]
11. Yang, Y.; Liu, X.; Zhu, Z.; Zhong, Y.; Bando, Y.; Golberg, D.; Yao, J.; Wang, X. The Role of Geometric Sites in 2D Materials for Energy Storage. *Joule* **2018**, *2*, 1075–1094. [[CrossRef](#)]
12. Tang, X.; Ye, H.; Liu, W.; Liu, Y.; Guo, Z.; Wang, M. Lattice-Distorted Lithiation Behavior of a Square Phase Janus MoSSe Monolayer for Electrode Applications. *Nanoscale Adv.* **2021**, *3*, 2902–2910. [[CrossRef](#)]
13. Bahari, Y.; Mortazavi, B.; Rajabpour, A.; Zhuang, X.; Rabczuk, T. Application of Two-Dimensional Materials as Anodes for Rechargeable Metal-Ion Batteries: A Comprehensive Perspective from Density Functional Theory Simulations. *Energy Storage Mater.* **2021**, *35*, 203–282. [[CrossRef](#)]
14. Zhang, H.; Yang, Y.; Ren, D.; Wang, L.; He, X. Graphite as Anode Materials: Fundamental Mechanism, Recent Progress and Advances. *Energy Storage Mater.* **2021**, *36*, 147–170. [[CrossRef](#)]
15. Tarascon, J.-M.; Armand, M. Issues and Challenges Facing Rechargeable Lithium Batteries. *Nature* **2001**, *414*, 359–367. [[CrossRef](#)]
16. Zhang, J.; Cao, H.; Tang, X.; Fan, W.; Peng, G.; Qu, M. Graphite/Graphene Oxide Composite as High Capacity and Binder-Free Anode Material for Lithium Ion Batteries. *J. Power Sources* **2013**, *241*, 619–626. [[CrossRef](#)]
17. Senyshyn, A.; Mühlbauer, M.J.; Dolotko, O.; Ehrenberg, H. Low-Temperature Performance of Li-Ion Batteries: The Behavior of Lithiated Graphite. *J. Power Sources* **2015**, *282*, 235–240. [[CrossRef](#)]
18. Wen, Y.; He, K.; Zhu, Y.; Han, F.; Xu, Y.; Matsuda, I.; Ishii, Y.; Cummings, J.; Wang, C. Expanded Graphite as Superior Anode for Sodium-Ion Batteries. *Nat. Commun.* **2014**, *5*, 4033. [[CrossRef](#)]
19. Stevens, D.A.; Dahn, J.R. The Mechanisms of Lithium and Sodium Insertion in Carbon Materials. *J. Electrochem. Soc.* **2001**, *148*, A803. [[CrossRef](#)]
20. Cao, Y.; Xiao, L.; Sushko, M.L.; Wang, W.; Schwenzler, B.; Xiao, J.; Nie, Z.; Saraf, L.V.; Yang, Z.; Liu, J. Sodium Ion Insertion in Hollow Carbon Nanowires for Battery Applications. *Nano Lett.* **2012**, *12*, 3783–3787. [[CrossRef](#)]
21. Moriwake, H.; Kuwabara, A.; Fisher, C.A.J.; Ikuhara, Y. Why Is Sodium-Intercalated Graphite Unstable? *RSC Adv.* **2017**, *7*, 36550–36554. [[CrossRef](#)]
22. Liu, Y.; Merinov, B.V.; Goddard, W.A. Origin of Low Sodium Capacity in Graphite and Generally Weak Substrate Binding of Na and Mg among Alkali and Alkaline Earth Metals. *Proc. Natl. Acad. Sci. USA* **2016**, *113*, 3735–3739. [[CrossRef](#)] [[PubMed](#)]
23. Chepkasov, I.V.; Ghorbani-Asl, M.; Popov, Z.I.; Smet, J.H.; Krasheninnikov, A.V. Alkali Metals inside Bi-Layer Graphene and MoS₂: Insights from First-Principles Calculations. *Nano Energy* **2020**, *75*, 104927. [[CrossRef](#)]
24. Jian, Z.; Luo, W.; Ji, X. Carbon Electrodes for K-Ion Batteries. *J. Am. Chem. Soc.* **2015**, *137*, 11566–11569. [[CrossRef](#)] [[PubMed](#)]
25. Tapia-Ruiz, N.; Armstrong, A.R.; Alptekin, H.; Amores, M.A.; Au, H.; Barker, J.; Boston, R.; Brant, W.R.; Brittain, J.M.; Chen, Y.; et al. 2021 Roadmap for Sodium-Ion Batteries. *J. Phys. Energy* **2021**, *3*, 031503. [[CrossRef](#)]
26. Xu, X.; Li, F.; Zhang, D.; Liu, Z.; Zuo, S.; Zeng, Z.; Liu, J. Self-Sacrifice Template Construction of Uniform Yolk-Shell ZnS@C for Superior Alkali-Ion Storage. *Adv. Sci.* **2022**, *9*, 2200247. [[CrossRef](#)]
27. Yuan, J.; Mu, M.; Xu, X.; Gan, Y.; He, H.; Zhang, X.; Li, X.; Kuang, F.; Li, H.; Liu, J. Three-Dimensional Porous FeS@N Doped Carbon Nanosheets for High-Rate and High-Stable Sodium/Potassium Storage. *Compos. Part B Eng.* **2022**, *247*, 110300. [[CrossRef](#)]
28. Chen, B.; Chao, D.; Liu, E.; Jaroniec, M.; Zhao, N.; Qiao, S.-Z. Transition Metal Dichalcogenides for Alkali Metal Ion Batteries: Engineering Strategies at the Atomic Level. *Energy Environ. Sci.* **2020**, *13*, 1096–1131. [[CrossRef](#)]
29. Yun, Q.; Li, L.; Hu, Z.; Lu, Q.; Chen, B.; Zhang, H. Layered Transition Metal Dichalcogenide-Based Nanomaterials for Electrochemical Energy Storage. *Adv. Mater.* **2020**, *32*, 1903826. [[CrossRef](#)]
30. He, H.; Lu, P.; Wu, L.; Zhang, C.; Song, Y.; Guan, P.; Wang, S. Structural Properties and Phase Transition of Na Adsorption on Monolayer MoS₂. *Nanoscale Res. Lett.* **2016**, *11*, 330. [[CrossRef](#)]
31. Wang, L.; Shih, E.-M.; Ghiotto, A.; Xian, L.; Rhodes, D.A.; Tan, C.; Claassen, M.; Kennes, D.M.; Bai, Y.; Kim, B.; et al. Correlated Electronic Phases in Twisted Bilayer Transition Metal Dichalcogenides. *Nat. Mater.* **2020**, *19*, 861–866. [[CrossRef](#)]
32. David, L.; Bhandavat, R.; Barrera, U.; Singh, G. Polymer-Derived Ceramic Functionalized MoS₂ Composite Paper as a Stable Lithium-Ion Battery Electrode. *Sci. Rep.* **2015**, *5*, 9792. [[CrossRef](#)]
33. Liu, T.; Jin, Z.; Liu, D.-X.; Du, C.; Wang, L.; Lin, H.; Li, Y. A Density Functional Theory Study of High-Performance Pre-Lithiated MS₂ (M = Mo, W, V) Monolayers as the Anode Material of Lithium Ion Batteries. *Sci. Rep.* **2020**, *10*, 6897. [[CrossRef](#)]
34. Mikhaleva, N.S.; Visotin, M.A.; Kuzubov, A.A.; Popov, Z.I. VS₂/Graphene Heterostructures as Promising Anode Material for Li-Ion Batteries. *J. Phys. Chem. C* **2017**, *121*, 24179–24184. [[CrossRef](#)]
35. Yang, F.; Feng, X.; Glans, P.-A.; Guo, J. MoS₂ for beyond Lithium-Ion Batteries. *APL Mater.* **2021**, *9*, 050903. [[CrossRef](#)]
36. Zhang, X.; Shi, H.; Liu, L.; Min, C.; Liang, S.; Xu, Z.; Xue, Y.; Hong, C.; Cai, Z. Construction of MoS₂/Mxene Heterostructure on Stress-Modulated Kapok Fiber for High-Rate Sodium-Ion Batteries. *J. Colloid Interface Sci.* **2022**, *605*, 472–482. [[CrossRef](#)]
37. Kulka, A.; Hanc, A.; Walczak, K.; Plotek, J.; Sun, J.; Lu, L.; Borca, C.; Huthwelker, T. Direct Evidence of an Unanticipated Crystalline Phase Responsible for the High Performance of Few-Layered-MoS₂ Anodes for Na-Ion Batteries. *Energy Storage Mater.* **2022**, *48*, 314–324. [[CrossRef](#)]
38. Barik, G.; Pal, S. 2D Square Octagonal Molybdenum Disulfide: An Effective Anode Material for LIB/SIB Applications. *Adv. Theory Simul.* **2020**, *3*, 2000157. [[CrossRef](#)]
39. Gavryushkin, P.; Sagatov, N.; Sukhanova, E.; Medrish, I.; Popov, Z. Janus Structures of SMoSe and SVSe Compositions with Low Enthalpy and Unusual Crystal Chemistry. *J. Appl. Cryst.* **2022**, *55*, 1324–1335. [[CrossRef](#)]

40. Zhang, J.; Xia, Y.; Wang, B.; Jin, Y.; Tian, H.; Ho, W.k.; Xu, H.; Jin, C.; Xie, M. Single-Layer Mo₅Te₈—A New Polymorph of Layered Transition-Metal Chalcogenide. *2D Mater.* **2020**, *8*, 015006. [[CrossRef](#)]
41. Wang, X.; Guan, X.; Ren, X.; Liu, T.; Huang, W.; Cao, J.; Jin, C. Deriving 2D M₂X₃ (M = Mo, W, X = S, Se) by Periodic Assembly of Chalcogen Vacancy Lines in Their MX₂ Counterparts. *Nanoscale* **2020**, *12*, 8285–8293. [[CrossRef](#)]
42. Chepkasov, I.V.; Sukhanova, E.V.; Kvashnin, A.G.; Zakaryan, H.A.; Aghamalyan, M.A.; Mamasakhlisov, Y.S.; Manakhov, A.M.; Popov, Z.I.; Kvashnin, D.G. Computational Design of Gas Sensors Based on V₃S₄ Monolayer. *Nanomaterials* **2022**, *12*, 774. [[CrossRef](#)] [[PubMed](#)]
43. Sukhanova, E.V.; Kvashnin, A.G.; Agamalyan, M.A.; Zakaryan, H.A.; Popov, Z.I. Map of Two-Dimensional Tungsten Chalcogenide Compounds (W–S, W–Se, W–Te) Based on USPEX Evolutionary Search. *JETP Lett.* **2022**, *115*, 292–296. [[CrossRef](#)]
44. Sukhanova, E.; Kvashnin, A.; Bereznikova, L.; Zakaryan, H.; Aghamalyan, M.; Kvashnin, D.; Popov, Z. 2D-Mo₃S₄ Phase as Promising Contact for MoS₂. *Appl. Surf. Sci.* **2022**, *589*, 152971. [[CrossRef](#)]
45. Kung, C.-W.; Han, P.-C.; Chuang, C.-H.; Wu, K.C.-W. Electronically Conductive Metal–Organic Framework-Based Materials. *APL Mater.* **2019**, *7*, 110902. [[CrossRef](#)]
46. Zou, G.; Hou, H.; Ge, P.; Huang, Z.; Zhao, G.; Yin, D.; Ji, X. Metal–Organic Framework-Derived Materials for Sodium Energy Storage. *Small* **2018**, *14*, 1702648. [[CrossRef](#)]
47. Dang, S.; Zhu, Q.-L.; Xu, Q. Nanomaterials Derived from Metal–Organic Frameworks. *Nat. Rev. Mater.* **2018**, *3*, 17075. [[CrossRef](#)]
48. Li, X.; He, C.; Zheng, J.; Ye, W.; Yin, W.; Tang, B.; Rui, Y. Preparation of Promising Anode Materials with Sn-MOF as Precursors for Superior Lithium and Sodium Storage. *J. Alloy. Compd.* **2020**, *842*, 155605. [[CrossRef](#)]
49. Hohenberg, P.; Kohn, W. Inhomogeneous Electron Gas. *Phys. Rev.* **1964**, *136*, B864–B871. [[CrossRef](#)]
50. Kohn, W.; Sham, L.J. Self-Consistent Equations Including Exchange and Correlation Effects. *Phys. Rev.* **1965**, *140*, A1133–A1138. [[CrossRef](#)]
51. Hafner, J. Ab-Initio Simulations of Materials Using VASP: Density-Functional Theory and Beyond. *J. Comput. Chem.* **2008**, *29*, 2044–2078. [[CrossRef](#)]
52. Kresse, G.; Furthmüller, J.; Hafner, J. Theory of the Crystal Structures of Selenium and Tellurium: The Effect of Generalized-Gradient Corrections to the Local-Density Approximation. *Phys. Rev. B* **1994**, *50*, 13181–13185. [[CrossRef](#)]
53. Kresse, G.; Furthmüller, J. Efficiency of Ab-Initio Total Energy Calculations for Metals and Semiconductors Using a Plane-Wave Basis Set. *Comput. Mater. Sci.* **1996**, *6*, 15–50. [[CrossRef](#)]
54. Kresse, G.; Furthmüller, J. Efficient Iterative Schemes for Ab Initio Total-Energy Calculations Using a Plane-Wave Basis Set. *Phys. Rev. B* **1996**, *54*, 11169–11186. [[CrossRef](#)]
55. Kresse, G.; Joubert, D. From Ultrasoft Pseudopotentials to the Projector Augmented-Wave Method. *Phys. Rev. B* **1999**, *59*, 1758–1775. [[CrossRef](#)]
56. Blöchl, P.E. Projector Augmented-Wave Method. *Phys. Rev. B* **1994**, *50*, 17953–17979. [[CrossRef](#)]
57. Perdew, J.P.; Burke, K.; Ernzerhof, M. Generalized Gradient Approximation Made Simple. *Phys. Rev. Lett.* **1996**, *77*, 3865–3868. [[CrossRef](#)]
58. Monkhorst, H.J.; Pack, J.D. Special Points for Brillouin-Zone Integrations. *Phys. Rev. B* **1976**, *13*, 5188–5192. [[CrossRef](#)]
59. Grimme, S.; Antony, J.; Ehrlich, S.; Krieg, H. A Consistent and Accurate Ab Initio Parametrization of Density Functional Dispersion Correction (DFT-D) for the 94 Elements H–Pu. *J. Chem. Phys.* **2010**, *132*, 154104. [[CrossRef](#)]
60. Henkelman, G.; Jónsson, H. Improved Tangent Estimate in the Nudged Elastic Band Method for Finding Minimum Energy Paths and Saddle Points. *J. Chem. Phys.* **2000**, *113*, 9978–9985. [[CrossRef](#)]
61. Henkelman, G.; Uberuaga, B.P.; Jónsson, H. A Climbing Image Nudged Elastic Band Method for Finding Saddle Points and Minimum Energy Paths. *J. Chem. Phys.* **2000**, *113*, 9901–9904. [[CrossRef](#)]
62. Togo, A.; Tanaka, I. First Principles Phonon Calculations in Materials Science. *Scr. Mater.* **2015**, *108*, 1–5. [[CrossRef](#)]
63. Eriksson, F.; Fransson, E.; Erhart, P. The Hiphive Package for the Extraction of High-Order Force Constants by Machine Learning. *Adv. Theory Simul.* **2019**, *2*, 1800184. [[CrossRef](#)]
64. Momma, K.; Izumi, F. VESTA 3 for Three-Dimensional Visualization of Crystal, Volumetric and Morphology Data. *J. Appl. Cryst.* **2011**, *44*, 1272–1276. [[CrossRef](#)]
65. Kumar, A.; Ahluwalia, P.K. Electronic Structure of Transition Metal Dichalcogenides Monolayers 1H-MX₂ (M = Mo, W; X = S, Se, Te) from Ab-Initio Theory: New Direct Band Gap Semiconductors. *Eur. Phys. J. B* **2012**, *85*, 186. [[CrossRef](#)]
66. Savin, A.; Nesper, R.; Wengert, S.; Fässler, T.F. ELF: The Electron Localization Function. *Angew. Chem. Int. Ed.* **1997**, *36*, 1808–1832. [[CrossRef](#)]
67. Lin, G.; Ju, Q.; Guo, X.; Zhao, W.; Adimi, S.; Ye, J.; Bi, Q.; Wang, J.; Yang, M.; Huang, F. Intrinsic Electron Localization of Metastable MoS₂ Boosts Electrocatalytic Nitrogen Reduction to Ammonia. *Adv. Mater.* **2021**, *33*, 2007509. [[CrossRef](#)]
68. Li, Y.; Li, Y.-L.; Araujo, C.M.; Luo, W.; Ahuja, R. Single-Layer MoS₂ as an Efficient Photocatalyst. *Catal. Sci. Technol.* **2013**, *3*, 2214–2220. [[CrossRef](#)]
69. Barik, G.; Pal, S. Defect Induced Performance Enhancement of Monolayer MoS₂ for Li- and Na-Ion Batteries. *J. Phys. Chem. C* **2019**, *123*, 21852–21865. [[CrossRef](#)]
70. Su, J.; Pei, Y.; Yang, Z.; Wang, X. Ab Initio Study of Graphene-like Monolayer Molybdenum Disulfide as a Promising Anode Material for Rechargeable Sodium Ion Batteries. *RSC Adv.* **2014**, *4*, 43183–43188. [[CrossRef](#)]